

# Quantitative microvascular hemoglobin mapping using visible light spectroscopic Optical Coherence Tomography

Shau Poh Chong, Conrad W. Merkle, Conor Leahy, Harsha Radhakrishnan, and Vivek J. Srinivasan\*

Biomedical Engineering Department, University of California Davis, Davis, CA 95616, USA  
\*vjsriniv@ucdavis.edu

**Abstract:** Quantification of chromophore concentrations in reflectance mode remains a major challenge for biomedical optics. Spectroscopic Optical Coherence Tomography (SOCT) provides depth-resolved spectroscopic information necessary for quantitative analysis of chromophores, like hemoglobin, but conventional SOCT analysis methods are applicable only to well-defined specular reflections, which may be absent in highly scattering biological tissue. Here, by fitting of the dynamic scattering signal spectrum in the OCT angiogram using a forward model of light propagation, we quantitatively determine hemoglobin concentrations directly. Importantly, this methodology enables mapping of both oxygen saturation and total hemoglobin concentration, or alternatively, oxyhemoglobin and deoxyhemoglobin concentration, simultaneously. Quantification was verified by *ex vivo* blood measurements at various pO<sub>2</sub> and hematocrit levels. Imaging results from the rodent brain and retina are presented. Confounds including noise and scattering, as well as potential clinical applications, are discussed.

©2015 Optical Society of America

**OCIS codes:** (110.4500) Optical coherence tomography; (170.3880) Medical and biological imaging.

## References and links

1. H. F. Zhang, K. Maslov, M. Sivaramakrishnan, G. Stoica, and L. H. V. Wang, "Imaging of hemoglobin oxygen saturation variations in single vessels in vivo using photoacoustic microscopy," *Appl. Phys. Lett.* **90**(5), 053901 (2007).
2. R. V. Kuranov, J. Qiu, A. B. McElroy, A. Estrada, A. Salvaggio, J. Kiel, A. K. Dunn, T. Q. Duong, and T. E. Milner, "Depth-resolved blood oxygen saturation measurement by dual-wavelength photothermal (DWP) optical coherence tomography," *Biomed. Opt. Express* **2**(3), 491–504 (2011).
3. B. Yin, R. V. Kuranov, A. B. McElroy, S. Kazmi, A. K. Dunn, T. Q. Duong, and T. E. Milner, "Dual-wavelength photothermal optical coherence tomography for imaging microvasculature blood oxygen saturation," *J. Biomed. Opt.* **18**(5), 056005 (2013).
4. U. Morgner, W. Drexler, F. X. Kärtner, X. D. Li, C. Pitris, E. P. Ippen, and J. G. Fujimoto, "Spectroscopic optical coherence tomography," *Opt. Lett.* **25**(2), 111–113 (2000).
5. R. Leitgeb, M. Wojtkowski, A. Kowalczyk, C. K. Hitzenberger, M. Sticker, and A. F. Fercher, "Spectral measurement of absorption by spectroscopic frequency-domain optical coherence tomography," *Opt. Lett.* **25**(11), 820–822 (2000).
6. D. J. Faber, E. G. Mik, M. C. Aalders, and T. G. J. M. van Leeuwen, "Oxygen saturation dependent index of refraction of hemoglobin solutions assessed by OCT," in *Biomedical Optics 2003*, (International Society for Optics and Photonics, 2003), pp. 271–281.
7. D. J. Faber, E. G. Mik, M. C. Aalders, and T. G. van Leeuwen, "Toward assessment of blood oxygen saturation by spectroscopic optical coherence tomography," *Opt. Lett.* **30**(9), 1015–1017 (2005).
8. L. Kagemann, G. Wollstein, M. Wojtkowski, H. Ishikawa, K. A. Townsend, M. L. Gabriele, V. J. Srinivasan, J. G. Fujimoto, and J. S. Schuman, "Spectral oximetry assessed with high-speed ultra-high-resolution optical coherence tomography," *J. Biomed. Opt.* **12**(4), 041212 (2007).

9. L. Wang, Z. Ding, L. Huang, and M. Geiser, "Numerical analysis on oxygen saturation measurement by dual-wavelength optical low-coherence interferometry," in *Fifth International Conference on Photonics and Imaging in Biology and Medicine*, (International Society for Optics and Photonics, 2007), pp. 65342S.
10. C. W. Lu, C. K. Lee, M. T. Tsai, Y. M. Wang, and C. C. Yang, "Measurement of the hemoglobin oxygen saturation level with spectroscopic spectral-domain optical coherence tomography," *Opt. Lett.* **33**(5), 416–418 (2008).
11. J. Yi and X. Li, "Estimation of oxygen saturation from erythrocytes by high-resolution spectroscopic optical coherence tomography," *Opt. Lett.* **35**(12), 2094–2096 (2010).
12. J. Yi, Q. Wei, W. Liu, V. Backman, and H. F. Zhang, "Visible-light optical coherence tomography for retinal oximetry," *Opt. Lett.* **38**(11), 1796–1798 (2013).
13. J. Yi, S. Chen, V. Backman, and H. F. Zhang, "In vivo functional microangiography by visible-light optical coherence tomography," *Biomed. Opt. Express* **5**(10), 3603–3612 (2014).
14. F. E. Robles, C. Wilson, G. Grant, and A. Wax, "Molecular imaging true-colour spectroscopic optical coherence tomography," *Nat. Photonics* **5**(12), 744–747 (2011).
15. D. J. Faber, E. G. Mik, M. C. Aalders, and T. G. van Leeuwen, "Light absorption of (oxy-)hemoglobin assessed by spectroscopic optical coherence tomography," *Opt. Lett.* **28**(16), 1436–1438 (2003).
16. X. Liu, K. Zhang, Y. Huang, and J. U. Kang, "Spectroscopic-speckle variance OCT for microvasculature detection and analysis," *Biomed. Opt. Express* **2**(11), 2995–3009 (2011).
17. M. Friebe, J. Helfmann, U. Netz, and M. Meinke, "Influence of oxygen saturation on the optical scattering properties of human red blood cells in the spectral range 250 to 2,000 nm," *J. Biomed. Opt.* **14**(3), 034001 (2009).
18. N. Bosschaart, G. J. Edelman, M. C. Aalders, T. G. van Leeuwen, and D. J. Faber, "A literature review and novel theoretical approach on the optical properties of whole blood," *Lasers Med. Sci.* **29**(2), 453–479 (2014).
19. R. N. Pittman, "In vivo photometric analysis of hemoglobin," *Ann. Biomed. Eng.* **14**(2), 119–137 (1986).
20. V. J. Srinivasan, S. P. Chong, C. Merkle, H. Radhakrishnan, and C. Leahy, "Optical Coherence Imaging of Hemodynamics, Metabolism, and Cell Viability during Brain Injury," in *CLEO: Applications and Technology*, (Optical Society of America, 2014), AF2B.2 (2014).
21. F. E. Robles, S. Chowdhury, and A. Wax, "Assessing hemoglobin concentration using spectroscopic optical coherence tomography for feasibility of tissue diagnostics," *Biomed. Opt. Express* **1**(1), 310–317 (2010).
22. S. P. Chong, C. W. Merkle, H. Radhakrishnan, C. Leahy, A. Dubra, Y. Sulai, and V. J. Srinivasan, "Optical Coherence Imaging of Microvascular Oxygenation and Hemodynamics," in *CLEO: Applications and Technology*, (Optical Society of America, 2014), AT10.2.
23. S. Prahl, "Optical Absorption of Hemoglobin", retrieved <http://omlc.ogi.edu/spectra/hemoglobin/>.
24. K. F. Palmer and D. Williams, "Optical properties of water in the near infrared," *J. Opt. Soc. Am.* **64**(8), 1107–1110 (1974).
25. G. S. Hong, S. Diao, J. L. Chang, A. L. Antaris, C. X. Chen, B. Zhang, S. Zhao, D. N. Atochin, P. L. Huang, K. I. Andreasson, C. J. Kuo, and H. J. Dai, "Through-skull fluorescence imaging of the brain in a new near-infrared window," *Nat. Photonics* **8**(9), 723–730 (2014).
26. F. Robles, R. N. Graf, and A. Wax, "Dual window method for processing spectroscopic optical coherence tomography signals with simultaneously high spectral and temporal resolution," *Opt. Express* **17**(8), 6799–6812 (2009).
27. S. Makita, T. Fabritius, and Y. Yasuno, "Full-range, high-speed, high-resolution 1 microm spectral-domain optical coherence tomography using BM-scan for volumetric imaging of the human posterior eye," *Opt. Express* **16**(12), 8406–8420 (2008).
28. L. H. Gray and J. M. Steadman, "Determination of the Oxyhaemoglobin Dissociation Curves for Mouse and Rat Blood," *J. Physiol.* **175**(2), 161–171 (1964).
29. M. Wojtkowski, V. Srinivasan, T. Ko, J. Fujimoto, A. Kowalczyk, and J. Duker, "Ultrahigh-resolution, high-speed, Fourier domain optical coherence tomography and methods for dispersion compensation," *Opt. Express* **12**(11), 2404–2422 (2004).
30. K. Briely-Sabo and A. Bjornerud, "Accurate de-oxygenation of ex vivo whole blood using sodium Dithionite," *Proc. Intl. Sot. Mag. Reson. Med.* **8**, 2025 (2000).
31. P. J. Drew, A. Y. Shih, J. D. Driscoll, P. M. Knutsen, P. Blinder, D. Davalos, K. Akassoglou, P. S. Tsai, and D. Kleinfeld, "Chronic optical access through a polished and reinforced thinned skull," *Nat. Methods* **7**(12), 981–984 (2010).
32. V. J. Srinivasan, H. Radhakrishnan, E. H. Lo, E. T. Mandeville, J. Y. Jiang, S. Barry, and A. E. Cable, "OCT methods for capillary velocimetry," *Biomed. Opt. Express* **3**(3), 612–629 (2012).
33. C. Xu, F. Kamalabadi, and S. A. Boppart, "Comparative performance analysis of time-frequency distributions for spectroscopic optical coherence tomography," *Appl. Opt.* **44**(10), 1813–1822 (2005).
34. R. N. Graf and A. Wax, "Temporal coherence and time-frequency distributions in spectroscopic optical coherence tomography," *J. Opt. Soc. Am. A* **24**(8), 2186–2195 (2007).
35. H. Radhakrishnan and V. J. Srinivasan, "Compartment-resolved imaging of cortical functional hyperemia with OCT angiography," *Biomed. Opt. Express* **4**(8), 1255–1268 (2013).
36. N. Bosschaart, T. G. van Leeuwen, M. C. Aalders, and D. J. Faber, "Quantitative comparison of analysis methods for spectroscopic optical coherence tomography," *Biomed. Opt. Express* **4**(11), 2570–2584 (2013).

37. M. Kraszewski, M. Trojanowski, and M. R. Strąkowski, "Comment on Quantitative comparison of analysis methods for spectroscopic optical coherence tomography," *Biomed. Opt. Express* **5**(9), 3023–3033 (2014).
38. N. Bosschaart, T. G. van Leeuwen, M. C. Aalders, and D. J. Faber, "Quantitative comparison of analysis methods for spectroscopic optical coherence tomography: reply to comment," *Biomed. Opt. Express* **5**(9), 3034–3035 (2014).
39. E. M. Hillman, "Optical brain imaging in vivo: techniques and applications from animal to man," *J. Biomed. Opt.* **12**(5), 051402 (2007).
40. F. C. Delori, "Noninvasive technique for oximetry of blood in retinal vessels," *Appl. Opt.* **27**(6), 1113–1125 (1988).
41. A. V. Hill, "The possible effects of the aggregation of the molecules of haemoglobin on its dissociation curves," *J. Physiol.* **40**, 7 (1910).
42. P. Cimalla, J. Walthers, M. Mittasch, and E. Koch, "Shear flow-induced optical inhomogeneity of blood assessed in vivo and in vitro by spectral domain optical coherence tomography in the 1.3  $\mu\text{m}$  wavelength range," *J. Biomed. Opt.* **16**(11), 116020 (2011).
43. D. J. Faber and T. G. van Leeuwen, "Are quantitative attenuation measurements of blood by optical coherence tomography feasible?" *Opt. Lett.* **34**(9), 1435–1437 (2009).
44. Y. Wang and R. Wang, "Autocorrelation optical coherence tomography for mapping transverse particle-flow velocity," *Opt. Lett.* **35**(21), 3538–3540 (2010).
45. N. V. Iftimia, D. X. Hammer, C. E. Bigelow, D. I. Rosen, T. Ustun, A. A. Ferrante, D. Vu, and R. D. Ferguson, "Toward noninvasive measurement of blood hematocrit using spectral domain low coherence interferometry and retinal tracking," *Opt. Express* **14**(8), 3377–3388 (2006).
46. V. J. Srinivasan and H. Radhakrishnan, "Optical Coherence Tomography angiography reveals laminar microvascular hemodynamics in the rat somatosensory cortex during activation," *Neuroimage* **102**(Pt 2), 393–406 (2014).
47. H. F. Zhang, K. Maslov, G. Stoica, and L. V. Wang, "Functional photoacoustic microscopy for high-resolution and noninvasive in vivo imaging," *Nat. Biotechnol.* **24**(7), 848–851 (2006).
48. S. Ogawa, R. S. Menon, D. W. Tank, S. G. Kim, H. Merkle, J. M. Ellermann, and K. Ugurbil, "Functional brain mapping by blood oxygenation level-dependent contrast magnetic resonance imaging. A comparison of signal characteristics with a biophysical model," *Biophys. J.* **64**(3), 803–812 (1993).
49. C. Du, N. D. Volkow, A. P. Koretsky, and Y. Pan, "Low-frequency calcium oscillations accompany deoxyhemoglobin oscillations in rat somatosensory cortex," *Proc. Natl. Acad. Sci. U.S.A.* **111**(43), E4677–E4686 (2014).
50. A. L. Vazquez, K. Masamoto, M. Fukuda, and S. G. Kim, "Cerebral oxygen delivery and consumption during evoked neural activity," *Front Neuroenergetics* **2**, 11 (2010).
51. A. L. Vazquez, M. Fukuda, M. L. Tasker, K. Masamoto, and S. G. Kim, "Changes in cerebral arterial, tissue and venous oxygenation with evoked neural stimulation: implications for hemoglobin-based functional neuroimaging," *J. Cereb. Blood Flow Metab.* **30**(2), 428–439 (2010).
52. ANSI Z136.1 - Safe Use of Lasers" (Laser Institute of America), retrieved 12.05.2014, 2014, <https://www.lia.org/publications/ansi/Z136-1>.
53. A. I. Srieenc, Z. L. Kurth-Nelson, and E. A. Newman, "Imaging retinal blood flow with laser speckle flowmetry," *Front. Neuroenergetics* **2**, 128 (2010).
54. P. Y. Teng, J. Wanek, N. P. Blair, and M. Shahidi, "Response of inner retinal oxygen extraction fraction to light flicker under normoxia and hypoxia in rat," *Invest. Ophthalmol. Vis. Sci.* **55**(9), 6055–6058 (2014).
55. D. J. Faber, M. C. Aalders, E. G. Mik, B. A. Hooper, M. J. van Gemert, and T. G. van Leeuwen, "Oxygen saturation-dependent absorption and scattering of blood," *Phys. Rev. Lett.* **93**(2), 028102 (2004).
56. R. Samatham, S. L. Jacques, and P. Campagnola, "Optical properties of mutant versus wild-type mouse skin measured by reflectance-mode confocal scanning laser microscopy (rCSLM)," *J. Biomed. Opt.* **13**(4), 041309 (2008).

## 1. Introduction

While many biomedical optical diagnostic and imaging techniques must be performed in reflectance mode, quantitative measurements of tissue chromophore concentrations using reflected light remain challenging. Methods such as photoacoustic microscopy (PAM) [1] and photothermal Optical Coherence Tomography (OCT) [2,3] quantify absorption in an excited volume, which can be related to chromophore concentration if multiple excitation wavelengths are used. To be truly quantitative, these methods require accounting for the possibly wavelength-dependent attenuation to and from the volume where absorption is to be measured. Alternatively, spectroscopic OCT (SOCT) [4–14] can determine depth-resolved spectra, from which quantification of chromophores based on spectroscopic analysis can then be achieved if the path length is known [15].

Early work on determining hemoglobin oxygenation with SOCT was mainly performed at near-infrared wavelengths [7,8,16], due in part to the high exposure limits of near-infrared light, high penetration depths of near-infrared light, and wide availability of suitable broadband near-infrared light sources and OCT systems. However, tissue and blood scattering are much higher than absorption at near-infrared wavelengths. As red blood cell scattering depends on wavelength, orientation, and oxygen saturation [17,18], quantification may be compromised. While tissue scattering is  $\sim 2\times$  higher at visible wavelengths compared to near-infrared wavelengths, hemoglobin absorption is more than one order of magnitude higher (Fig. 1). Thus, absorption is expected to play a more prominent role in the attenuation characteristics of the OCT signal at visible wavelengths than at near-infrared wavelengths. Hence, the contribution of hemoglobin absorption to the optical density of small vessels will be considerably larger at visible wavelengths, mitigating scattering confounds and enabling the quantification of hemoglobin in smaller vessels [19]. Recent work using visible wavelength OCT has shown the feasibility of achieving saturation measurements using both parametric [12,20,21] and non-parametric approaches [13,22].

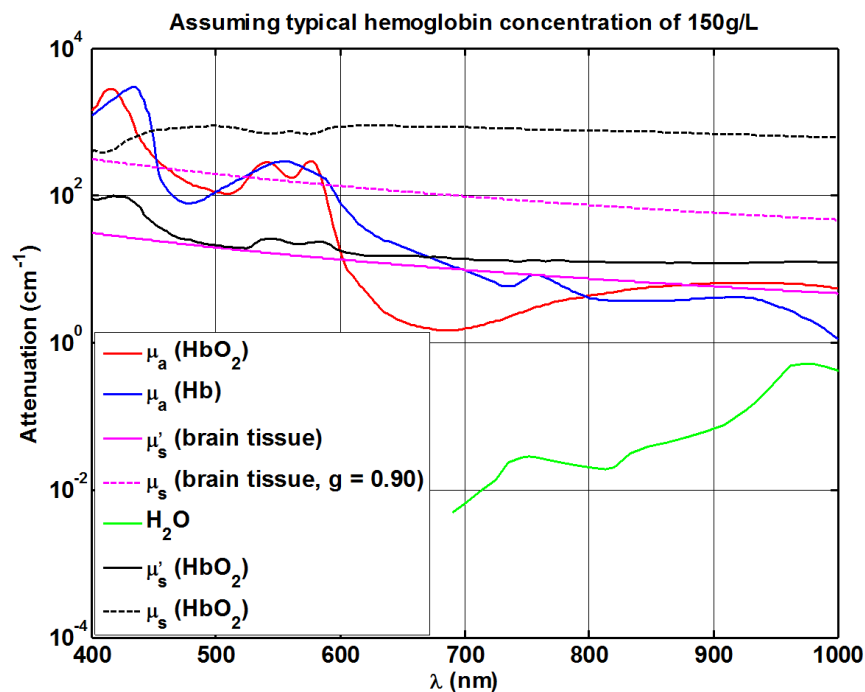


Fig. 1. Wavelength-dependence of oxyhemoglobin and deoxyhemoglobin absorption (red and blue, respectively), whole blood scattering (black), brain tissue scattering (pink), and water absorption (green). Hemoglobin absorption spectra and blood scattering spectra (compiled averages from literature) were obtained from [23] and [18] respectively. The water absorption spectrum was obtained from [24] while the reduced scattering coefficient of brain tissue was obtained from [25], and the scattering coefficient was derived assuming a constant anisotropy of  $g=0.9$ . As shown in the plot, hemoglobin absorption is more significant relative to scattering in the visible wavelength range, as compared to the near-infrared wavelength range.

Spectroscopic OCT can be performed by taking Fourier transforms of windowed spectral regions [4] to form a series of depth-resolved images at different center wavelengths, or by performing a short-time Fourier transform of the complex signal to determine spectra at different depths [16]. Both methods result in spectrograms which can be analyzed using either parametric [12,20,21] or non-parametric [16] methods. Dual-window approaches [14,26] can be described as performing two separate short-time Fourier transforms and combining the

results. However, conventional SOCT analysis methods require the isolation of specular reflections from which a spectrum can be directly derived [4,5]. Such methods are challenging to apply in biological tissue because backscattering from biological tissue is seldom specular. Rather, multiple scattering centers within a single resolution element add with random phases to form a wavelength-dependent speckle pattern. This speckle pattern, if not accounted for, prevents reliable chromophore estimates.

Here we present a novel method of generating and analyzing spectroscopic OCT data based on isolating the dynamic scattering power spectrum from a vessel. This method fits a model to the intravascular spectra to quantify hemodynamic parameters directly. Mapping of hemoglobin content and saturation in vessels is demonstrated. Issues related to spectral estimation, including scattering confounds and noise bias, are discussed. The method is validated in rat blood at physiological blood gas values and a range of hematocrit values. Finally, *in vivo* applications of quantitative hemoglobin mapping are shown.

## 2. Experimental methods

### 2.1 System description

A high-speed visible light spectral/Fourier domain spectroscopic OCT system (SOCT) (Fig. 2) was constructed for *in vivo* imaging of rodents.

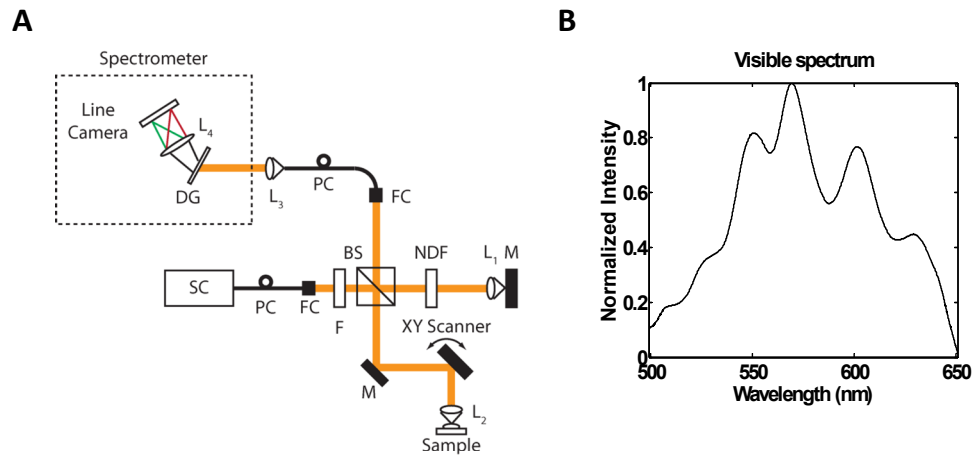


Fig. 2. A) Visible light SOCT setup. The supercontinuum source (SC) delivered the light via a photonic crystal (PC) fiber. FC: fiber collimator; F: spectral filters; BS: beam splitter; M: mirror; NDF: neutral density filter; DG: diffraction grating;  $L_{1,3}$ : 30mm achromatic doublets;  $L_4$ : 75 mm achromatic doublet pairs. The figure is not drawn to scale. B) Spectrum measured by spectrometer after filtering of the SC light source.

The system used an unpolarized supercontinuum light source (SuperK EXW-12, NKT Photonics) with a collimated output beam of 600  $\mu\text{m}$  diameter. The output beam was first attenuated by 96% using a reflection off a glass block and spectrally filtered such that the spectral range centers at 575 nm. In the OCT setup, the light was first split by an anti-reflection coated non-polarizing 50/50 beam splitter into the sample and reference arms of a Michelson interferometer. In the sample arm, the beam was raster scanned by a 2D galvanometer scanner (6210H, Cambridge Technology) before being focused by an achromatic doublet with a 30 mm focal length, resulting in a focused spot size of about 21.6  $\mu\text{m}$  (i.e. FWHM  $\sim 0.37\lambda/\text{NA}$ ) at the focal plane. The reference arm contained a variable neutral density filter (NDF) to adjust the reference power and an achromatic doublet identical to the one in the sample arm for balancing the dispersion. The back-reflected beams from both arms are combined by the beam splitter and collected by a collimator-coupled single mode

photonic crystal fiber (FD7, NKT Photonics) with a mode field diameter of about 4.2  $\mu\text{m}$  at 532 nm. The output of the photonic crystal fiber was directed to a custom-made spectrometer. The output from the fiber was collimated to a beam of about 5 mm diameter by using another 30 mm achromatic doublet. A volume transmission grating (1800 l/mm, Wasatch Photonics) and lens (75 mm achromatic doublet pair), and a complementary metal-oxide semiconductor (CMOS) line-scan camera (Basler SPL 4096-140km, Germany) were used in the spectrometer. The acquisition window of the line camera was set to 2560 pixels in order to achieve a line rate of about 90 kHz, with a duty cycle up to 85%. The calibrated spectral sampling interval of the system was 0.0612 nm, which provided an imaging depth of 1.35 mm in air, or 1.05  $\mu\text{m}$  per pixel. The camera was connected to a frame grabber (PCIe-1433, National Instruments, Austin, Texas), and triggered by a NI 6351 digital I/O board (National Instruments, Austin, Texas) which also controlled the 2D galvanometer scanner. The acquisition was controlled by a custom LabVIEW® program that allowed various scanning patterns/rates and fields of view (FOV). Unless otherwise mentioned, the average power at the sample for imaging was around 1 mW.

## 2.2 System calibration

Spectroscopic fitting methods are very sensitive to small errors or offsets in wavelength. Moreover, sampling must be uniformly spaced in wavenumber before Fourier transformation to achieve optimal sensitivity roll-off and axial resolution. Thus, careful calibration of the spectrometer was performed by a sequence of two sets of measurements: 1) External narrowband light sources at known wavelengths were coupled to the spectrometer through the reference arm to provide *absolute* wavenumber calibration at a set of discrete pixel locations. 2) The phase of the interference spectrum [27] was used to provide *relative* wavenumber calibration across the whole spectrometer. Information from the absolute (1) and relative (2) calibration measurements was then integrated using a fitting procedure.

The interference spectrum captured by the line scan camera can be described as

$$S[k(x_i)] \cos\{2k(x_i)z + \varphi_{disp}[k(x_i)]\}, \quad (1)$$

where  $k = 2\pi/\lambda$  is the wavenumber;  $x_i$  are the positions of each pixel on the line scan camera, i.e.  $i = 1, \dots, N_p$ ;  $N_p$  is the total number of pixels in the line scan camera; and  $S$  is the interference spectrum envelope. The phase of the cosine term comprises a  $z$ -dependent part  $2k(x_i)z$  and a  $z$ -independent part  $\varphi_{disp}[k(x_i)]$ . Though grating-based spectrometers provide samples that are approximately uniformly spaced in wavelength, in practice, nonlinearities in the grating equation may become significant across a wide spectral range.  $\varphi_{disp}[k(x)]$  is the depth-independent phase offset introduced by the wavelength-dependent path length difference in the interferometer, typically caused by dispersion mismatch. Although negligible for our interferometer (Fig. 2), this term is included for completeness. This phase offset can be cancelled out by subtracting measured phases of two spectral fringe patterns obtained at different path length differences, as described in Ref [27]. Then, the resultant phase difference  $\Delta\varphi(x_i)$  of two measured spectral fringes is related to wavenumber  $k(x_i)$  by the following expression:

$$\Delta\varphi(x_i) = 2k(x_i)\Delta z + \varphi_{offset}, \quad (2)$$

where  $\Delta z$  is the known separation depth of the two spectral fringe patterns. Due to the fact that the two depths were measured sequentially, an unknown phase offset  $\varphi_{offset}$  is included in the above equation to account for the total phase evolution between the two positions of the reference arm. As the phase difference  $\Delta\varphi(x_i)$  is linear in wavenumber  $k$ , with a known constant of proportionality, the wavenumber is determined up to this phase offset from the

phase measurements alone. If the phase offset is known, the position-dependent wavenumber  $k(x_i)$  of the spectrometer can be determined from:

$$k(x_i) = \frac{\Delta\varphi(x_i) - \varphi_{\text{offset}}}{2\Delta z}. \quad (3)$$

Using narrowband calibration light sources with known center wavelengths, the following additional measurements were obtained:

$$k_c(x_n) \approx \frac{2\pi}{\lambda_n} \quad n = 1, \dots, N, \quad (4)$$

where  $N$  is the number of calibration wavelengths. Two calibration wavelengths were chosen for this study. The unknown  $\varphi_{\text{offset}}$ , the total phase evolution between the two positions of the reference arm, could not be directly determined due to phase noise. Therefore, it was instead fit based on minimizing the sum of squared errors between the  $k(x_n)$  values (i.e. Eq. (3)) and the  $k_c(x_n)$  (i.e. Eq. (4)) obtained from calibration light sources.

$$\hat{\varphi}_{\text{offset}} = \arg \min_{\varphi_{\text{offset}}} \sum_{n=1}^N [k(x_n) - k_c(x_n)]^2. \quad (5)$$

The wavelengths corresponding to each pixel on the line scan camera,  $\lambda(x_i)$ , necessary for spectroscopic analysis; could then be estimated by

$$\hat{k}(x_i) = \frac{\Delta\varphi(x_i) - \hat{\varphi}_{\text{offset}}}{2\Delta z}, \quad \hat{\lambda}(x_i) = \frac{2\pi}{\hat{k}(x_i)}. \quad (6)$$

Fitting the calibration wavelengths under the assumption that spectrometer sampling was linear in wavelength (Fig. 3(A)-3(B), blue dashed line), led to a sub-optimal roll-off performance (Fig. 3(C), blue dashed line). If linear sampling in wavelength was assumed and the bandwidth was empirically chosen to optimize the roll-off (Fig. 3(A)-3(B), green dashed line), incorrect spectral calibration (Fig. 3(A), green dashed line) and depth calibration (Fig. 3(C), green dashed line) resulted. By contrast, the calibration procedure described above resulted in accurate spectral calibration (Fig. 3(A)-3(B), red line) and optimal roll-off (Fig. 3(D), red line). Thus, the above calibration procedure comprising the two sets of measurements was performed after each experiment.

### 2.3 Ex vivo calibration setup

In order to validate the spectroscopic measurements, rat blood flowing through fluorinated ethylene propylene (FEP) tubing was imaged (Fig. 4). The corresponding  $\text{SO}_2$  values were estimated by SOCT as described below. Fresh blood was harvested from Long Evans rats (Charles River, MA) by cardiac puncture and mixed with a few drops of sodium heparin to prevent coagulation. Sodium fluoride (Fisher Scientific) was also added into the blood (one drop of 1% NaF/3mL blood) to slow down the rate of glycolysis of blood, and thereby stabilize the pH [28]. The blood sample was then placed in a closed induction chamber with variable gas supply (i.e.  $\text{N}_2$ ,  $\text{O}_2$  and  $\text{CO}_2$ ) to maintain the carbon dioxide partial pressure ( $\text{pCO}_2$ ) of the blood at around 40 mmHg while varying the oxygen partial pressure ( $\text{pO}_2$ ) of the blood. The  $\text{pCO}_2$  in the closed chamber was monitored by a micro-capnograph (Columbus Instruments, USA). A magnetic stirrer was used to ensure that the sample rapidly reached equilibrium with the surrounding gas mixture in approximately 15 minutes. After equilibration, a few hundred microliters of blood were extracted from the chamber in a syringe. The pH and blood gas of the blood were measured using a blood gas analyzer (RAPIDLab® 248, Siemens Healthcare). Then, the blood sample was transferred using the syringe and pumped through the FEP tubing (inner diameter of 200  $\mu\text{m}$ ) for imaging under the

SOCT system. Another measurement of the blood gases was taken again after the imaging session to confirm that the blood gases were not altered by the exposure to atmospheric air. Measurements were rejected if the pre-imaging and post-imaging blood gas measurements differed by more than 10 mm Hg in  $pO_2$  or if the  $pCO_2$  and pH values fell outside of the physiological range. Throughout the experiment, the pH and  $pCO_2$  of the blood sample were maintained within a physiological range (pH  $\sim 7.35 - 7.45$ ;  $pCO_2 \sim 35-45$  mmHg). This was crucial to accurately estimate  $SO_2$  from  $pO_2$  and a single oxyhemoglobin dissociation curve (OHDC). The results are shown in Fig. 5.

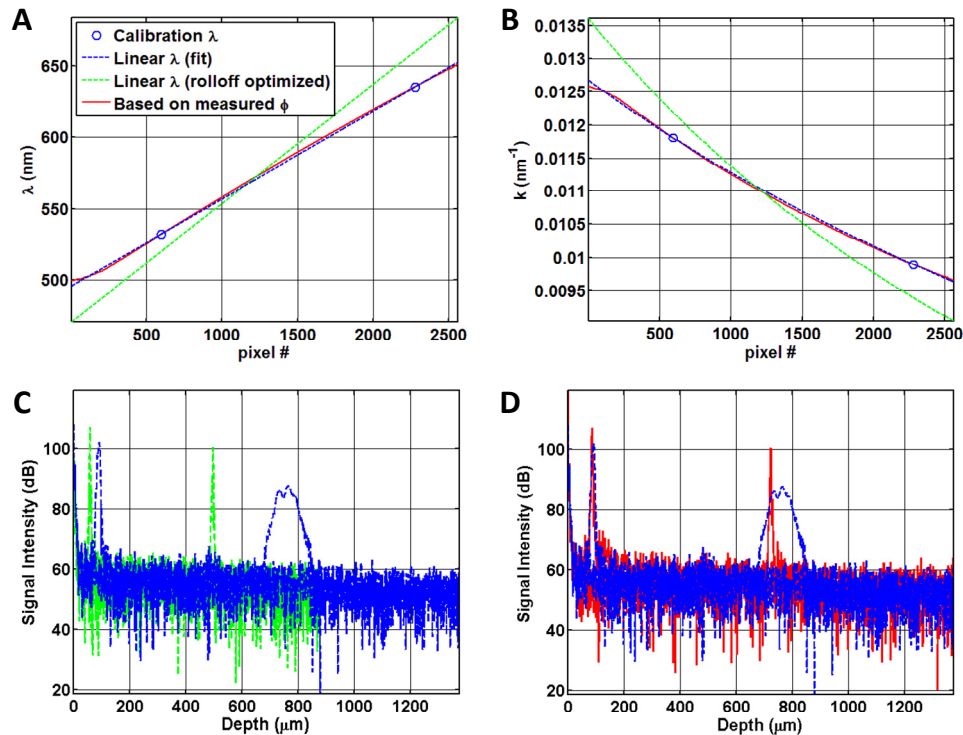


Fig. 3. Spectrometer calibration requires correct accounting for nonlinearities in wavelength sampling. A) The locations of two calibration wavelengths were determined using auxiliary laser diodes with central wavelengths at 532 nm and 635 nm respectively (blue circles show calibration wavelengths). The linear wavelength fit is shown as a blue dashed line. Another linear wavelength curve, empirically chosen to optimize sensitivity roll-off, is plotted (green dashed line). Finally, the calibrated curve, derived from both the measured phase and calibration wavelengths, is shown (red solid line; see description in article for details). B) Wavenumbers corresponding to wavelengths (A) are shown. C) The axial profiles of two spectral fringe patterns after resampling based on the linear wavelength fit, followed by Fourier transformation, are shown (blue dashed line). Poor sensitivity roll-off and axial profile broadening were observed at larger depths, indicating incorrect resampling. By contrast, by empirically stretching the linear wavelength curve, improved roll-off could be achieved, at the expense of inaccurate calibration (green dashed line). D) Using our proposed calibration procedure, axial profiles show good sensitivity roll-off and negligible broadening (red solid line). Furthermore, unlike empirical linear wavelength calibration (green dashed line in A), calibrated wavelengths matched the two calibration wavelengths (red solid line in A).

To validate the feasibility of accessing hemoglobin concentration using SOCT, we then diluted the blood sample to achieve different hematocrits using isotonic saline solution (B. Braun Inc., Irvine, USA) and imaged the diluted blood flowing through FEP tubing using SOCT. Three metrics were then investigated, including the OCT signal slope, maximum OCT



signal, and fitting of the spectroscopic data based on the modified Beer-Lambert Law described in Sections 3.2.7 and 3.2.8. The results are shown in Fig. 6.

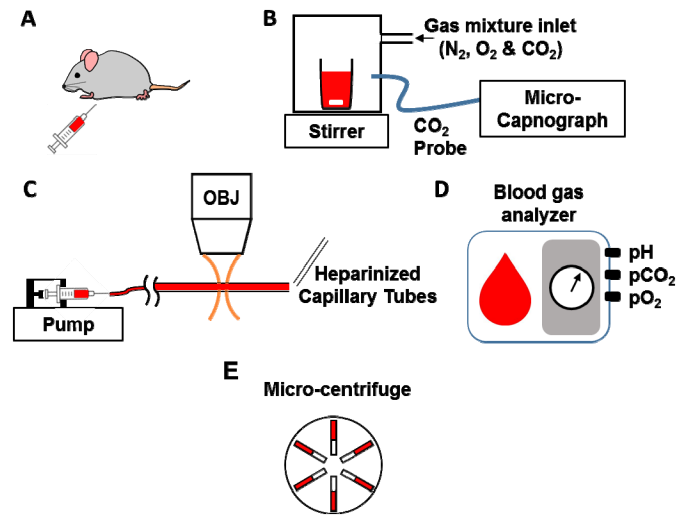


Fig. 4. A) Fresh whole blood was harvested from Long Evans rats by cardiac puncture. B) Blood samples were placed in a closed chamber with a gas mixture supply (i.e.  $N_2$ ,  $O_2$ , &  $CO_2$ ) to maintain physiological  $pCO_2$  levels and to manipulate  $pO_2$  levels. The blood sample was stirred by a magnetic stirrer to ensure homogenous mixing of the blood and equilibration with the surrounding gas mixture. C) Each blood sample was pumped through FEP tubing (inner diameter of 200  $\mu m$ ) and imaged under the SOCT system. D) Blood gas and pH readings were taken before and after imaging sessions to confirm physiological  $pCO_2$  (35-45 mmHg) and pH (7.35-7.45). Low  $pO_2$  values were achieved by adding sufficient sodium dithionite to fully deoxygenate the hemoglobin [30]. E) The hematocrit of the blood sample was measured using a micro-centrifuge.

#### 2.4 Preparation and in vivo experiments

For retinal imaging, wild-type rats (N=3, Male, 200-250 g, Long Evans, Charles River Lab, MA) were used. During the experiment, the rat was supplied a mixture of isoflurane, medical air and oxygen through a ventilation system (VetEquip. Inc, Pleasanton, CA). The rat was first anesthetized in an induction chamber supplied with 2-2.25% v/v isoflurane in a gas mixture of 80% air and 20% oxygen. The total gas flow provided was set at 1.5 L/min. After the rat was under deep anesthesia, it was immobilized on a stereotaxic frame (Stoelting Co., IL) or a custom made head mount throughout the experiment. The rat was cyclopleged with 1% tropicamide to dilate the iris. 2% lidocaine was also injected into the peribulbar space to reduce eyeball movement. During retinal imaging using SOCT, a cover slip was gently placed on the cornea with goniosol.

For brain imaging, wild-type mice (N=3, Male, 24-29 g, C57BL/6, Charles River Lab, MA) were used. During the experiment, the mouse was supplied a mixture of isoflurane, medical air and oxygen through a ventilating system (VetEquip. Inc, Pleasanton, CA). The mouse was first anesthetized in an induction chamber supplied with 1.25-1.5% v/v isoflurane with a gas mixture of 80% air and 20% oxygen. The total gas flow provided was set at 1.5 L/min. After the mouse was under deep anesthesia, it was immobilized on a stereotactic frame (Stoelting Co., IL) or a custom-made head mount. Artificial teardrops were applied to the eyes to prevent corneal dehydration. Then, a thinned-skull window was created over the parietal cortex [31] for imaging. During imaging, the mouse was fixed on a stereotactic frame or a custom-made head mount in order to reduce the motion artifacts caused by breathing.

All the experiment procedures and protocols were reviewed and approved by UC Davis Institutional Animal Care and Use Committee (IACUC).

## 2.5 Data acquisition

The scanning protocol sampled each location in a 3D volume over time by acquiring 100 repeated B-scans, each consisting of 512 A-scans. The optical spectrum corresponding to each A-scan was focused onto a line camera (Basler SPL 4096-140km, Germany) with the acquisition window set to 2,560 lateral pixels with vertical binning. The scanning was then repeated at 256 y-locations, giving a 4D data set with dimensions of  $512 \times 256 \times 2560 \times 100$ .

## 2.6 Complex image reconstruction

Spline interpolation was employed to resample the interferograms to be uniformly sampled in wavenumber. As described above, careful calibration of the spectrometer was performed after each experiment to precisely determine the wavenumber corresponding to every pixel on the camera. A dispersion compensation method was also implemented [29]. The resampled and dispersion-corrected interferograms were Fourier transformed to obtain the complex depth-resolved A-scans.

## 3. Data processing

For the data processing description, we consider only the analysis of a single set of repeated cross-sectional images at a fixed y-location. This corresponds to a set of complex amplitudes,  $a$ , as a function of transverse position ( $x$ ), depth ( $z$ ), and time ( $t$ ). It is understood that volumetric data sets can be synthesized by acquiring and processing sequences of such image sets at different y locations.

### 3.1 Axial motion correction

Axial motion, if much lower in amplitude than the axial resolution, may be accounted for by computing and correcting for a phase shift ( $\delta\theta$ ). On the other hand, axial motion on the order of the axial resolution requires correcting for a bulk axial image shift ( $\delta z$ ) in addition to the phase shift. Due to the micron-scale axial resolution in this study, both of these effects must be accounted for. The corrected OCT signal  $a'$  for the A-scan at position  $x$  was obtained from the following expression, where  $a$  represents the complex OCT signal.

$$a'(x, z, t) = a[x, z - \delta z(x, t), t] e^{-j\delta\theta(x, t)}. \quad (7)$$

### 3.2 Signal model and estimation

To describe our method, we extend a previous description of the complex OCT signal [32] to include spectroscopic ( $\lambda$  or  $k = 2\pi/\lambda$ ) dependence. Here we obtain a rapid time-series of complex OCT images, or B-scans at 176 Hz. The complex, motion-corrected OCT signal,  $a'$ , can be considered as the superposition of a static component ( $a'_s$ ), a dynamic component ( $a'_d$ ), and an additive noise component ( $a'_n$ ) [32], i.e.

$$a'(x, z, t, k) = a'_s(x, z, k) + a'_d(x, z, t, k) + a'_n(x, z, t, k). \quad (8)$$

At any given voxel, these three components are assumed to be independent complex random processes. Therefore, the three components of the complex OCT signal give rise to three corresponding additive components in the signal intensity ( $I$ ).

$$I(x, z, k) = I_s(x, z, k) + I_d(x, z, k) + I_n(z, k). \quad (9)$$

The power in the dynamic scattering component ( $I_d$ ) is related to red blood cell content, while the static scattering component ( $I_s$ ) is related to tissue scattering.  $I_n$  denotes the noise power, and is assumed to be independent of transverse position ( $x$ ).

### 3.2.1 Short-time Fourier transform (STFT)

In spectroscopic OCT, the usual analysis methods applied to OCT data, such as the Fourier transform, are insufficient due to the inherent loss of spectral information associated with the transformation from the wavenumber domain to the spatial domain. Instead, one must use localized spectral analysis methods to obtain a joint distribution of both spatial and spectral information [33,34]. The discrete-time short-time Fourier transform (STFT) generates a function of depth ( $z$ ) and its conjugate variable, wavenumber ( $k$ ), from a function of depth ( $z$ ).

$$F(z, k) = STFT\{f(z)\} = \sum_{z'} f(z') w(z' - z) e^{-j2kz'}. \quad (10)$$

The factor of 2 in the exponent is due to the double-pass delay. The window function  $w(z)$  defines the tradeoff between spatial and spectral resolution [35]. A number of window functions have been employed for the purpose of achieving an optimal trade-off between spatial and spectral information for spectroscopic analysis [26]. Good spatial resolution is desirable in order to localize the spectroscopic information as much as possible, thus enabling smaller vessels to be adequately probed in the analysis. On the other hand, to ensure good fitting the spectral resolution should be sufficient to discern the characteristic features of the hemoglobin extinction spectra. Prior studies have shown that rectangular windows lead to improved fidelity in representing hemoglobin spectral features [36–38] when using the STFT. The size of the rectangular STFT window in this study was chosen to be 21 pixels, corresponding to approximately 22  $\mu\text{m}$  axially (which is comparable to the transverse resolution of  $\sim 21.6 \mu\text{m}$ ). This yields a spectral resolution of approximately 7 nm, which was deemed sufficient to obtain an adequate representation of the Q bands in the absorbance spectrum.

### 3.2.2 Absorbance spectrum

The measured single-pass absorbance, constructed from SOCT data, can be most generally described according to the formula:

$$\hat{A}(x, z, k) = -\frac{1}{2} \ln \left[ \frac{\hat{I}_{vessel}(x, z, k)}{\hat{I}_{norm}(z, k)} \right], \quad (11)$$

where  $\hat{A}(x, z, k)$  is the estimated absorbance spectrum at a particular location within the sample. This is the measurement term that includes the effects of hemoglobin absorption. Ideally the only difference between the vessel spectrum (numerator,  $\hat{I}_{vessel}$ ) and normalization spectrum (denominator,  $\hat{I}_{norm}$ ) are the effects of hemoglobin absorption. A number of possible choices for the vessel spectrum and normalization spectrum are possible, each with advantages and disadvantages. Specific methods for this study are described below.

### 3.2.3 Vessel spectrum

The vessel spectrum ( $\hat{I}_{vessel}$ ) is computed via a short-time Fourier transform (STFT) algorithm. The dynamic scattering power can be estimated through filtering the complex OCT signal in time with a high-pass filter kernel  $h_{hpf}(t)$ , i.e.,

$$\hat{I}_{vessel}(x, z, k) = \hat{I}_d(x, z, k) = \sum_t \left| STFT\{h_{hpf}(t) * a'(x, z, t)\} \right|^2 - \hat{I}_{d,bkgnd}(z, k), \quad (12)$$

where  $*$  denotes convolution in time.  $\hat{I}_{d,bkgnd}$  denotes the estimate of the bias spectrum determined from the background, as described below in Eq. (14). If the filter parameters and inter-frame time are chosen appropriately, the resultant dynamic spectrum will be mostly insensitive to red blood cell (RBC) velocity changes and will therefore depend mostly on

RBC content [35]. For a two-frame complex difference method, this requires that the acquisition times of the two frames be separated by more than the decorrelation time. Here, a high-pass filter with a 3 dB cutoff frequency of 66 Hz was used. The estimated background spectrum is subtracted to avoid bias in the spectrum estimation, as described further below.

### 3.2.4 Normalization spectrum

The normalization spectrum is also obtained from the STFT of the OCT intensity data. We approximate the normalization spectrum ( $\hat{I}_{norm}$ ) as the static spectrum (averaged over a number of pixels,  $N_x$ , in  $x$ -dimension) as shown below:

$$\hat{I}_{norm}(z, k) = \hat{I}_s(z, k) = \frac{1}{N_x} \sum_x \left[ \sum_t \left| STFT \{ h_{hpf}(t) * a'(x, z, t) \} \right|^2 - \hat{I}_{s,bkgnd}(z, k) \right]. \quad (13)$$

Typically,  $h_{hpf} = I - h_{hpf}$  is chosen for convenience.  $\hat{I}_{s,bkgnd}$  denotes the estimate of the bias spectrum determined from the background, as described below in Eq. (15). Ideally, the sole difference between the normalization spectrum and the vessel spectrum is the fact that the vessel spectrum is influenced by blood attenuation across a vessel of interest. The normalization spectrum should theoretically account for a non-uniform source spectral shape and sample losses due to absorption or scattering outside the vessel of interest, as well as potentially, the spectral dependence of backscattering (assuming that the backscattering in the reference region approximates that of blood). For retinal imaging, the outer retina was excluded when determining the normalization spectrum due to the presence of photopigment and other chromophores. Other choices for the normalization spectrum include the reference arm spectrum or the interference spectrum at the depth of interest, obtained from calibration measurements on the spectrometer.

### 3.2.5 Bias correction

Since maximum permissible exposure (MPE) limits are smaller and sources are noisier in the visible wavelength range than in the near-infrared range, OCT signal-to-noise ratios are comparatively low at visible wavelengths. The operation of squaring a spectrum with additive noise before averaging results in a bias that persists asymptotically even when the number of averages is large. However, assuming that this noise is uncorrelated with the signal, this bias can be removed using a straightforward estimation and subtraction procedure. Rather than develop a theoretical description of the noise, we note that the noise spectrum is in general, dependent on axial position. This noise spectrum is estimated using an identical filtering and STFT approach that was applied for the static and dynamic spectra, but applied to a background region of the image or a separate set of reference frames. If a background region at a given desired depth is unavailable, the background at other depths can be used to determine the background at the desired depth based on a simple linear model. The respective bias spectra, estimated from the background, must be subtracted from both the vessel spectrum and the normalization spectrum before the division and normalization operations. The equations below parallel Eq. (12) and Eq. (13) above, and describe how the complex OCT signal from the background,  $a_{bkgnd}$ , is used to determine the bias for the dynamic and static spectra.

$$\hat{I}_{d,bkgnd}(z, k) = \sum_t \left| STFT \{ h_{hpf}(t) * a_{bkgnd}(z, t) \} \right|^2, \quad (14)$$

$$\hat{I}_{s,bkgnd}(z, k) = \sum_t \left| STFT \{ h_{hpf}(t) * a_{bkgnd}(z, t) \} \right|^2. \quad (15)$$

### 3.2.6 Speckle averaging

Our spectroscopic model for absorption and scattering is intended to fit to the average intensity at each wavelength. As speckle results in random interference effects, spectra must be incoherently ensemble averaged to estimate average intensity at each wavelength. Note that the electromagnetic field has a different speckle pattern for each optical frequency component; this results in a modulation of the OCT signal as a function of wavelength. An efficient scanning protocol resamples the same transverse location at a time interval on the order of or greater than the complex speckle decorrelation time, enabling the acquisition of independent data from many transverse locations in parallel. As high-resolution spectroscopic mapping in vessels is desirable, we choose to estimate the vessel spectrum ( $\hat{I}_{vessel}$ ) by averaging in time (Eq. (12)). By comparison, we choose to average the normalization spectrum ( $\hat{I}_{norm}$ ) in space (Eq. (13)), as the normalization spectrum that arises from static tissue is time-invariant and the normalization spectrum does not need to be determined with high resolution.

### 3.2.7 Fitting to determine saturation

To obtain values for blood oxygenation, we fit the measured absorbance spectrum (Eq. (11)) to a parametric model of light propagation, based on the modified Beer-Lambert Law. Neglecting focusing effects, the absorbance  $A$  takes the form

$$A(x, z, k) = \int C_{HbT}(x, z') \{ S(x, z') \epsilon_{HbO_2}(k) + [1 - S(x, z')] \epsilon_{Hb}(k) \} dz' + \Phi(x, z). \quad (16)$$

An integral over the axial direction is used to calculate the total absorbance. Assuming only a single vessel with a constant saturation and hemoglobin concentration, we obtain:

$$A(x, z, k) = C_{HbT}(x) L(x, z) \{ S(x) \epsilon_{HbO_2}(k) + [1 - S(x)] \epsilon_{Hb}(k) \} + \Phi(x, z), \quad (17)$$

where  $L$  is the single-pass distance travelled through the vessel,  $C_{HbT}$  is the total hemoglobin concentration,  $S$  is the oxygen saturation, and  $\epsilon$  denotes the molar extinction coefficient. Alternatively, this expression can be written in terms of chromophore concentrations ( $C_{HbO_2}$  and  $C_{Hb}$ ):

$$A(x, z, k) = L(x, z) [ C_{HbO_2}(x) \epsilon_{HbO_2}(k) + C_{Hb}(x) \epsilon_{Hb}(k) ] + \Phi(x, z), \quad (18)$$

$\Phi$  is a term related to scattering (including orientation effects) and may be modified to be wavelength-dependent [39]. We can rewrite Eq. (18) to describe the estimated absorbance:

$$\hat{A}(x, z, k) = a_1(x, z) \epsilon_{HbO_2}(k) + a_2(x, z) \epsilon_{Hb}(k) + a_3(x, z) + n(x, z, k). \quad (19)$$

A noise or error term  $n(x, z, k)$  has been included to account for the fact that the absorbance estimate is used. We employ a least-squares approximation to determine the parameters  $a_1 \sim LC_{HbO_2}$ ,  $a_2 \sim LC_{Hb}$ , and  $a_3 \sim \Phi$ . The  $a_3$  term is retained to improve the quality of the fit by accounting for the influence of scattering, as per Eq. (18). This influence is assumed to be weak compared to absorption over the range of illumination wavelengths [40], and so  $a_3$  was independent of  $\lambda$ . A simple power-law model can also be used to incorporate the attenuation due to scattering as a pseudo-chromophore [12]. In practice,  $a_3$  is useful to account for differences in scattering due to RBC orientation. Molar extinction coefficients were obtained from interpolation of published data [23] from wavelength to wavenumber. The fit was restricted to a range of 510 nm to 640 nm to exclude artifacts at the edges of the spectral

range. At each point, the absorbance spectrum is estimated as per Eq. (11) and fit as per Eq. (19). The oxygen saturation can then be obtained using  $S = a_1 / (a_1 + a_2)$ .

### 3.2.8 Quantitative total hemoglobin measurements

Using the model described in Eq. (18), it is also possible to directly determine molar hemoglobin concentration, or  $C_{HbT}$ . Comparing Eq. (18) and Eq. (19), we note the correspondence between the model parameters and chromophores as

$$a_1 \sim LC_{HbT}S = LC_{HbO_2}, \quad (20)$$

$$a_2 \sim LC_{HbT}(1-S) = LC_{Hb}. \quad (21)$$

Taking the sum of these parameters, we obtain

$$a_1 + a_2 \sim LC_{HbT}. \quad (22)$$

Thus, the quantity  $a_1 + a_2$  relates only to the single-pass path length and the total hemoglobin concentration along this path. As stated above,  $L$  is the single-pass distance through the vessel, while  $C_{HbT}$  is the molar hemoglobin concentration. As oxygenation was appropriately accounted for in the fitting procedure, this measure should not depend on oxygen saturation.

### 3.2.9 Mapping

Although SOCT allows spectroscopic information to be obtained from anywhere in an imaged sample, our model (Eq. (18)) applies only to blood vessels, where hemoglobin is present. Building from the localized measurement procedure described above, we aim to build a map of oxygen saturation over a range of vasculature. To achieve this, we first select a particular region-of-interest (ROI) from the tissue. This can be done in the *en face* plane, using a maximum intensity projection of the angiogram as a guide. This provides the  $x$ - $y$  localization of a particular ROI. To obtain the depth ( $z$ ) localization, we use the  $R^2$  metric of fitting as a guide. In general, the highest  $R^2$  values are found where hemoglobin is present (i.e., at a location within a blood vessel). Within a given vessel, the most accurate oxygenation values are found where  $LC_{HbT}$  is highest (i.e., where the cumulative hemoglobin absorption is highest). Thus, for a given  $x$ - $y$  location in the *en face* plane, we choose the corresponding A-scan and apply the fitting procedure to the absorbance spectrum at every depth  $z$  where the value of the angiogram exceeds a predetermined threshold. The desired depth,  $z_0$ , is then obtained from

$$z_0(x) = \arg \max_z \left\{ R^2 \left[ \hat{A}(x, z, k) \right] \right\}, \quad (23)$$

by finding the value of  $z$  for which  $R^2$  is maximized. To build the map of oxygen saturation, this procedure is repeated for each  $x$ - $y$  location within the selected ROI.

### 3.2.10 Image display

All parameters, including  $R^2$ ,  $LC_{HbT}$ ,  $LC_{Hb}$ ,  $LC_{HbO_2}$ ,  $\Phi$ , and saturation ( $S$ ), were determined in three-dimensions. For display of the various parameters as *en face* images, the value at depth  $z_0$  (Eq. (23)) with  $R^2 > 0.9$  (typically corresponding to the maximum value of  $LC_{HbT}$ ) was used.

## 4. Results

### 4.1 Ex vivo blood validation results

In Fig. 5(A), the  $pO_2$  values (mm Hg) and corresponding  $SO_2$  values (%) measured by SOCT are shown for *ex vivo* blood samples (red squares). An OHDC was fit to the data using the Hill

equation [41]. For comparison, the  $\text{SO}_2$  values,  $\text{pO}_2$  values, and OHDC for *ex vivo* rat blood from Gray & Steadman [28] are shown (blue circles). In Fig. 5(B), the  $\text{SO}_2$  values estimated by SOCT are plotted against the  $\text{SO}_2$  values predicted from  $\text{pO}_2$  values and the OHDC derived from Gray & Steadman's data [28]. A strong linear correlation ( $R^2 = 0.9232$ ;  $p\text{-value} < 10^{-5}$ ) is observed.

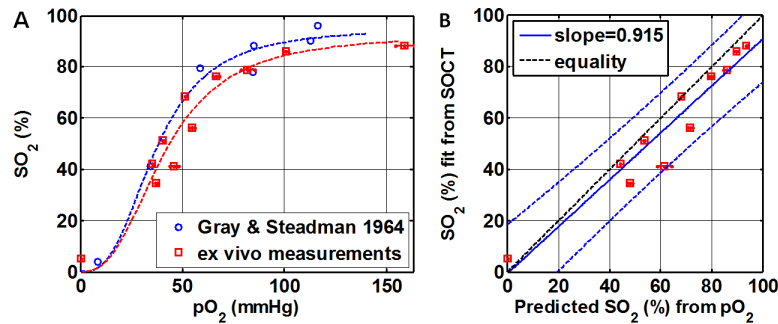


Fig. 5. Validation of *ex vivo* rat blood oxygen saturation measured using visible light SOCT. A) Estimated  $\text{SO}_2$  (%) using SOCT was plotted versus the corresponding  $\text{pO}_2$  measurements from a blood gas analyzer. The oxygen-hemoglobin dissociation curve (OHDC) was fit using the Hill equation [41] for our data set as well as Gray & Steadman's data [28]. B) There is a strong linear correlation between the  $\text{SO}_2$  values estimated by SOCT and those determined from  $\text{pO}_2$  and the OHDC fit of Gray & Steadman's data [28]. The 95% confidence intervals are plotted as dashed blue lines.

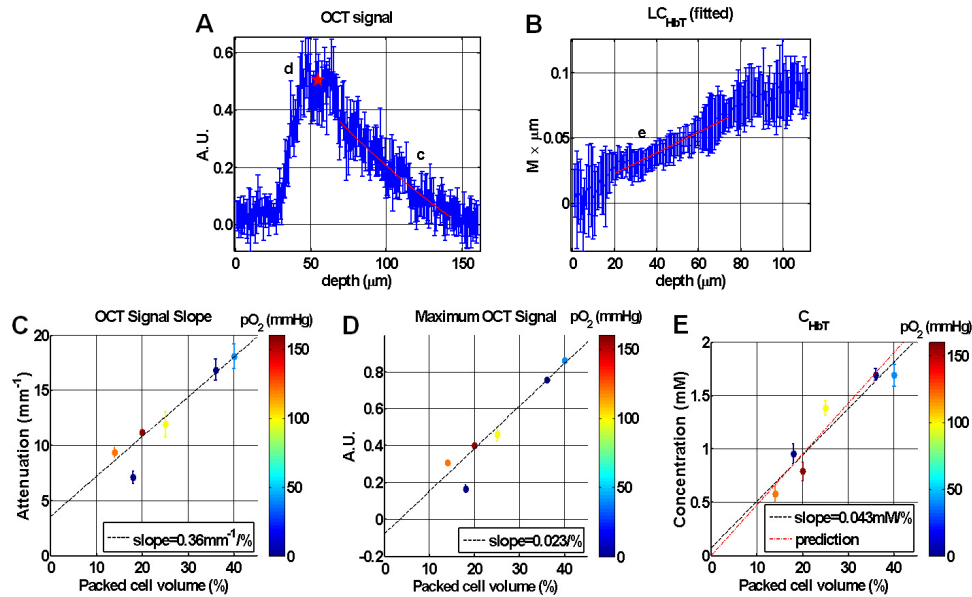


Fig. 6. *Ex vivo* calibration with rat blood shows a linear relationship between packed cell volume and attenuation slope (A, C), maximum OCT signal (A, D), and hemoglobin concentration obtained by fitting of the modified Beer-Lambert Law (B, E). The  $y$ -intercept of the fit of OCT signal slope vs. hematocrit (C) does not pass through the origin, indicating that the two quantities are not strictly proportional. Notably, the maximum OCT signal (D) and modified Beer-Lambert Law fitting (E) are proportional to hematocrit. However, in flowing blood, red blood cell orientation effects make signal slope and maximum signal (related to attenuation and backscattering, respectively) poor correlates of hemoglobin content [42]. The predicted line in E (red dashed line) is based on typical rat blood hematocrit of 45% and hemoglobin concentration of 138 g/L.

In Fig. 6, various metrics for hematocrit based on non-spectroscopic (A) and spectroscopic (B) methods are shown. The OCT signal slope (C, related to scattering and absorption), maximum OCT signal (D, related to backscattering), and hemoglobin concentration based on fitting the modified Beer-Lambert Law to spectroscopic data (E) are linearly related to hematocrit (packed cell volume). However, the OCT signal slope is not directly proportional to hematocrit as the regression line does not pass through the origin (Fig. 6(C)). As discussed further below, both the OCT signal slope (Fig. 6(C)) and maximum OCT signal (Fig. 6(D)) may be challenging to apply at high shear rates *in vivo* due to RBC orientation effects. The concentration values in Fig. 6(E) are obtained using the modified Beer-Lambert Law as a forward model, and agree quantitatively with prediction (red dashed line).

#### 4.2 *In vivo* imaging results

As cumulative hemoglobin ( $LC_{HbT}$ ) was the most robust measurement, the interpretation of this data was established first. Total hemoglobin mapping of the rat inner retina is shown in Fig. 7 and Fig. 8. In particular, depth-resolved analysis of the OCT signal from a rat inner retinal vessel (Fig. 7(A)) shows that red blood cell (RBC) orientation effects result in a stereotypical scattering pattern within vessels, with higher scattering at the top and bottom of the vessel (Fig. 7(B)) where RBCs are oriented with the flat face towards the incident light [42]. When depth-resolved fitting is performed (Fig. 7(C)) according to Eq. (19), the quantity  $LC_{HbT}$  starts at zero above the vessel and increases monotonically and almost linearly within the vessel to reach a final value below the vessel. This behavior agrees well with the physical model of light propagation (Eq. (19)), because the total double-pass path length through hemoglobin in the vessel increases as the depth increases. In particular, as shown in Fig. 7(C), the slope of the quantity  $LC_{HbT}$ , when plotted vs. depth, is the local hemoglobin concentration. Alternatively, the average hemoglobin concentration in the vessel may be determined from the measurement of  $LC_{HbT}$  at the distal end of the vessel, and dividing by the known vessel diameter. Using this estimation procedure, a hemoglobin concentration of 2.14 mM is estimated. This concentration is equivalent to 138 g/L, which corresponds to a hematocrit of 45%. In contrast to other *ad hoc* estimation procedures [43] that required separate calibration to obtain absolute values, the values presented here are based on known absorption properties of blood.

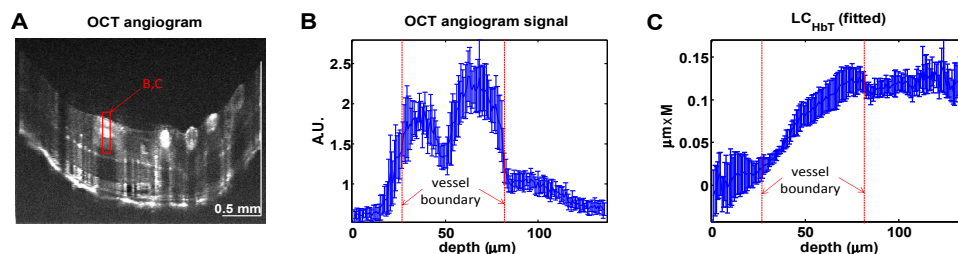


Fig. 7. Quantification of total hemoglobin concentration ( $C_{HbT}$ ) in the rat inner retina using axial profile of parameters obtained from spectroscopic fitting. A) OCT angiogram with a red box containing the axial scans used to determine axial profiles in B-C. B) The signal from the angiogram shows orientation effects with higher backscattering near the vessel walls due to orientation of RBCs in shear flow. C) Fitting to determine the path length times the hemoglobin concentration ( $LC_{HbT}$ ) yields a profile that is flat above the vessel, linearly increases inside the vessel, then flattens out below the vessel. The slope of  $LC_{HbT}$  within the vessel is quantitatively related to the local hematocrit, and is relatively insensitive to orientation effects.

Correspondingly, when the fitting procedure is applied pointwise at all locations in the cross-sectional image (Fig. 8) the highest  $R^2$  values are seen near the bottom of vessels where the model is most robust (Fig. 8(A)). Moreover,  $LC_{HbT}$  exhibits a characteristic “crescent” shape, also exhibiting the highest values near the distal tip of the vessel with the largest path length (Fig. 8(B)). The absorption MIP (based on the maximum intensity projection of the



quantity  $LC_{HbT}$ ) shows much more uniform values than the scattering MIP (based on the maximum intensity projection of the angiogram), which is confounded by orientation effects as well as vignetting (Fig. 8(C)-8(D)).

Figure 9 and Fig. 10 show images of the fitting parameters obtained from the mouse brain in cross-section and *en face* views, respectively. Figure 11 and Fig. 12 show images of the fitting parameters obtained from the rat retina in cross-section and *en face* views, respectively. Notable features that are common to these data sets include clear distinctions in saturation between arteries and veins in the *en face* views (Fig. 10(C) and Fig. 12(A)), increasing cumulative hemoglobin ( $LC_{HbT}$ ) from the proximal to distal end of vessels (Fig. 9(F) and Fig. 11(B)), significant cumulative oxyhemoglobin ( $LC_{HbO_2}$ ) in both arteries and veins (Fig. 9(D), Fig. 10(D), Fig. 11(C), and Fig. 12(C)), significant cumulative deoxyhemoglobin ( $LC_{Hb}$ ) only in veins (Fig. 9(E), Fig. 10(E), Fig. 11(D), and Fig. 12(D)), and maximal cumulative hemoglobin ( $LC_{HbT}$ ) proportional to vessel size (Fig. 10(F) and Fig. 12(B)).

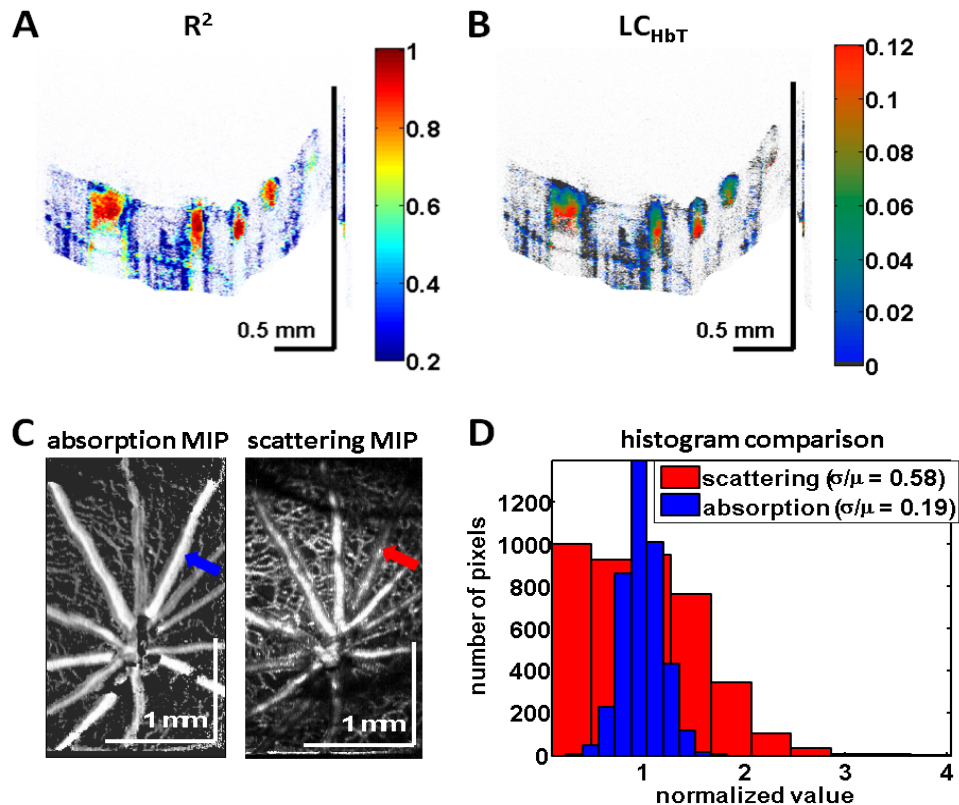


Fig. 8.  $C_{HbT}$  mapping of the rat inner retina. A)  $R^2$  from the fit of the absorbance spectrum of inner retinal vessels. Note that the largest  $R^2$  values are observed near the bottom of large vessels. B) Map of  $LC_{HbT}$  showing the largest values near the bottom of large vessels where the cumulative path length is largest. C) Comparison of absorption MIP (maximum intensity projection of  $LC_{HbT}$  over the axial direction) and scattering MIP (maximum intensity projection of standard angiogram, obtained by high-pass filtering along the slow axis). The absorption MIP shows more self-consistent values along large vessels. D) Comparison of histograms for absorption and scattering angiograms along a vessel (blue and red arrows in C) shows a threefold lower coefficient of variation using the absorption-based method. This is likely because the standard angiogram is sensitive to RBC orientation and vignetting effects, whereas the absorption-based angiogram is not.

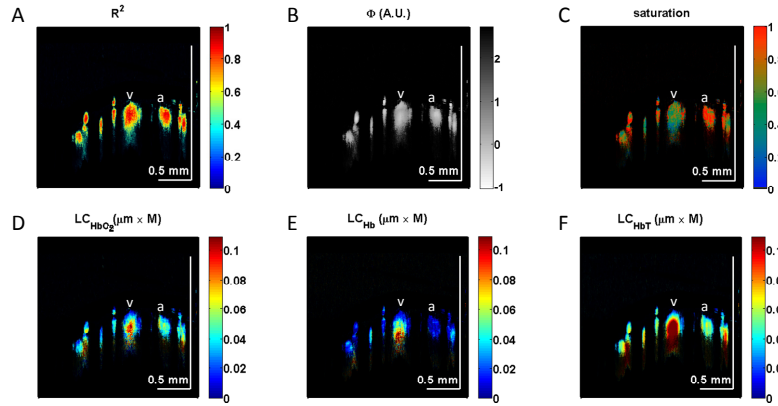


Fig. 9. Quantification of chromophores in the mouse neocortex in cross-section. A)  $R^2$  values from the fit (Eq. (19)) show the highest values near the distal side of vessels, with a decrease in  $R^2$  in the multiple scattering tails. B) The parameter  $\Phi$  accounts for RBC scattering effects. C) Saturation map, showing clear distinctions between arteries and veins. D-E) Maps of the product of oxygenated or deoxygenated hemoglobin concentrations and distance exhibit a characteristic downward “crescent” shape, due to larger cumulative distances at the distal end of the vessel. F) Similarly the product of total hemoglobin concentration and distance shows an increase with depth until the distal end of the vessel, and remains constant in the multiple scattering tail. All maps were displayed with transparency based on the local  $R^2$  value after averaging over six adjacent transverse ( $y$ ) locations. An artery (a) and vein (v) are labelled.

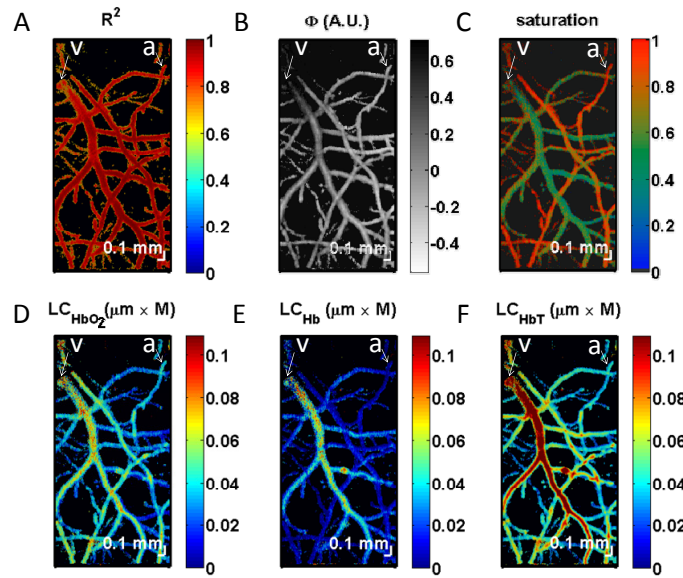


Fig. 10. Quantification of chromophores in the mouse brain in an *en face* view. A) Maximum intensity projection of  $R^2$  values from the fit (Eq. (19)) shows the highest values near the centers of vessels, with a decrease at the edges. B) The parameter  $\Phi$  accounts for RBC scattering effects. C) Saturation map, showing clear distinctions between arteries and veins. D) Map of the maximum of the product of oxygenated hemoglobin concentration and distance shows that veins and arteries contain oxyhemoglobin. E) By comparison, under the given experimental conditions, most of the deoxyhemoglobin is contained in veins. F) The map of the maximum of the product of total hemoglobin concentration and distance shows larger values in larger vessels, with localized increases at vessel crossings. It should be noted that quantitative measurements of chromophores can be achieved by integrating the maps (D-F) in the transverse plane ( $x$  and  $y$  dimensions). All maps were displayed with transparency based on the local  $R^2$  values at each transverse location, averaged over depth. An artery (a) and vein (v) are labelled.

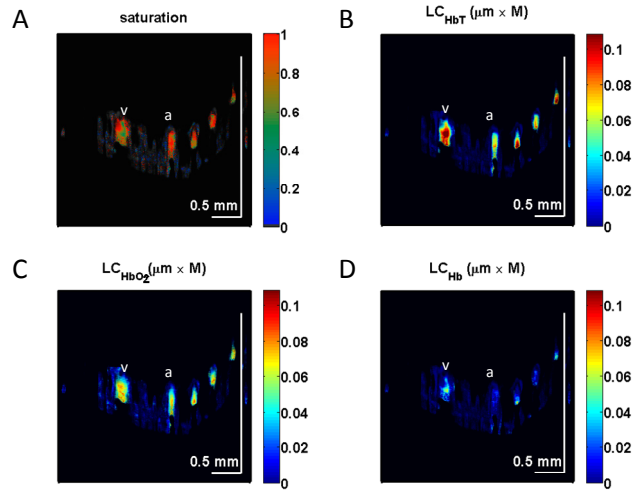


Fig. 11. Quantification of chromophores in the rat retina in cross-section. A) Saturation map, showing clear distinctions between arteries and veins. B) The product of total hemoglobin concentration and distance shows an increase with depth until the distal end of the vessel, and remains constant in the multiple scattering tail. C-D) Maps of the product of oxygenated or deoxygenated hemoglobin concentrations and distance increase towards the distal end of the vessel. While all vessels contain oxyhemoglobin (C), the three locations in D) with significant deoxyhemoglobin absorption at the distal end of the vessel correspond to veins. All maps were displayed using an alpha map based on the local  $R^2$  value after averaging over six adjacent transverse ( $y$ ) locations. An artery (a) and vein (v) are labelled.

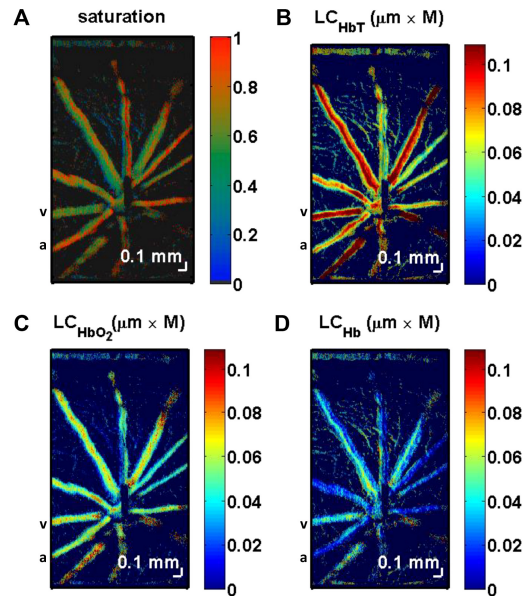


Fig. 12. Quantification of chromophores in the rat retina in an *en face* view. A) Saturation map, showing clear distinctions between arteries and veins. B) The map of the maximum of the product of total hemoglobin concentration and distance shows larger values in larger vessels. C) Map of the maximum of the product of oxygenated hemoglobin concentration and distance shows that veins and arteries contain oxyhemoglobin. D) By comparison, under the given experimental conditions, most of the deoxyhemoglobin is contained in veins. It should be noted that quantitative measurements of chromophores can be achieved by integrating the maps (B-D) in the transverse plane ( $x$  and  $y$  dimensions). All maps were displayed using an *en face* alpha map based on the local  $R^2$  values at each transverse location, averaged over depth.

As a demonstration of saturation mapping, Fig. 13 shows oxygen delivery from an artery to surrounding tissue. A minimum  $R^2$  threshold of 0.6 for the fit was used as a criterion for inclusion of saturation values. Figure 14 confirms that oxygen saturation is reduced to zero while all oxyhemoglobin is converted to deoxyhemoglobin after cardiac arrest. Figure 14 confirms that oxygen saturation is reduced to zero while all oxyhemoglobin is converted to deoxyhemoglobin after cardiac arrest.

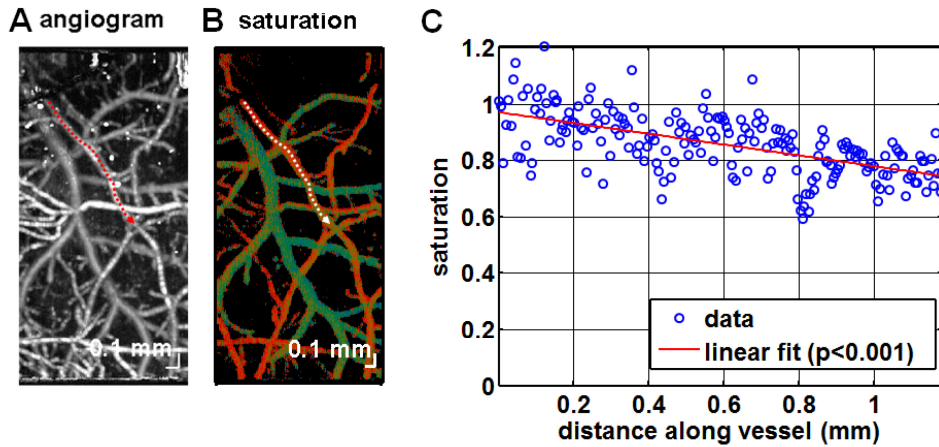


Fig. 13. Delivery of oxygen from an artery to surrounding tissue is demonstrated by high-resolution mapping. The oxygen saturation is parametrically determined as a function of distance along the flow direction shown as a dotted line on the angiogram (A) and saturation map (B). C) A statistically significant linear decrease in saturation along the direction of flow is demonstrated. Saturations from fits with an  $R^2$  value of  $>0.6$  were included for this figure.

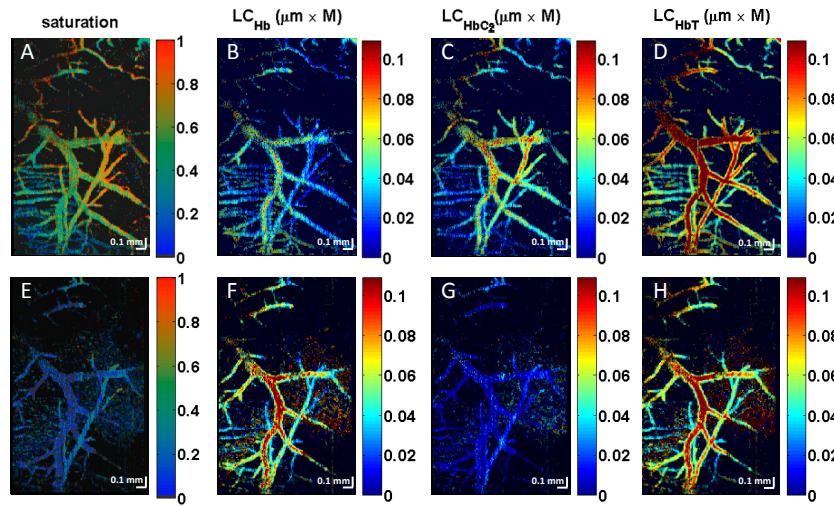


Fig. 14. Changes in intravascular oxygenation and chromophore concentrations after cardiac arrest. A-D) Maps of saturation, deoxyhemoglobin, oxyhemoglobin, and total hemoglobin at baseline. E-H) Maps of the same parameters after cardiac arrest. In particular, the saturation is reduced to zero (A,E) and deoxyhemoglobin content increases (B,F), while oxyhemoglobin is eliminated from the brain vasculature (C,G).

## 5. Discussion and conclusions

### 5.1 HbT mapping

The hemoglobin molecule is primarily responsible for the high oxygen carrying capacity of mammalian blood. Hence, the hemoglobin content of microvessels (in addition to flow) is a

key feature in their capacity to deliver oxygen to surrounding tissue. As blood cells are highly scattering at infrared and near-infrared wavelengths, previous attempts used OCT to quantify red blood cell content based on scattering. Methods of quantifying red blood cell content based on fluctuations in backscattering [44], or attenuation due to scattering [45] have been demonstrated. However, due to the highly anisotropic RBC shape, scattering properties depend on RBC orientation. Moreover, RBCs deform and systematically orient under shear flow [42], leading to a characteristic “hourglass” backscattering pattern in large vessels. Although *relative* measurements of backscattering may be related to concentration under certain circumstances [46], scattering characteristics (including backscatter and attenuation) may not be good metrics of *absolute* red blood cell concentration if orientation effects are not accounted for.

Here, we introduce a method for quantifying the total hemoglobin ( $LC_{HbT}$ ) along a given path by mapping total hemoglobin absorption. Absorption-based angiograms are more uniform and less sensitive to RBC orientation and vignetting than scattering-based angiograms (Fig. 8(C)-8(D)). As the path length is directly resolved, and vessels are directly visualized, it is possible to estimate or infer  $L$ , the optical path length corresponding to a given vessel. Thus, it is also possible to directly determine  $C_{HbT}$ , or the molar hemoglobin concentration. Hence, analogous to photoacoustic microscopy [47], microvascular imaging with absorption contrast is feasible using spectroscopic OCT. Moreover, by integrating a map of the maximal  $LC_{HbT}$  (e.g. Fig. 10(F) or Fig. 12(B)) over the transverse dimensions ( $x$  and  $y$ ), it is possible to determine the total amount of hemoglobin contained in a given region of interest. To our knowledge, such direct optical measurements of chromophore concentrations have not been possible heretofore due to the inability to directly determine path length.

### 5.2 $HbO_2$ mapping

Although it is not typically quantified directly, oxyhemoglobin is directly responsible for the oxygen content of blood under most physiological conditions. Thus quantification of oxyhemoglobin concentration in equivalents,  $[HbO_2]=4C_{HbO_2}$ , in combination with flow, can determine oxygen flux, or oxygen delivery. Oxygen fluxes to and from a defined region of tissue in steady state can be used to infer tissue oxygen consumption.

### 5.3 $Hb$ mapping

The Blood-oxygen-level dependent (BOLD) functional Magnetic Resonance Imaging (fMRI) signal is mainly due to changes in deoxyhemoglobin concentration [48]; however, methods of quantifying absolute  $Hb$  concentrations with optical imaging have been challenging, although relative changes in deoxyhemoglobin are readily accessible with optical methods [49]. We anticipate that the capability to perform absolute measurements of hemoglobin content will allow us to directly predict the BOLD signal from optical measurements alone in the rodent brain, enabling a range of mechanistic studies that will help to understand contributions of different vascular compartments to the BOLD signal.

### 5.4 Saturation mapping

Figure 13 shows that the spatial resolution enabled by quantitative saturation mapping enables assessment of oxygen delivery from microvasculature to surrounding tissue. While the raw data show significant scatter and occasionally exceed 1, a linear fit to the data versus parametric distance along the vessel (Fig. 13(C), red line) yields arterial saturation values in agreement with prior reports [50,51]. It is important to note that the saturation mapping approach as presented here does not account for physiological variations including those induced by flow pulsatility; hence some of the variance in our data may be physiological in nature. New scanning protocols and data acquisition schemes that do not assume ergodicity will address this issue in the future.

### 5.5 Potential clinical applications

While quantitative accuracy of spectroscopic OCT in the visible wavelength range demonstrated here strongly supports further investigation, the lower permissible light exposures [52] represent an important issue to consider for clinical applications. The data acquired here were obtained at the ~1 mW level, while clinical applications in ophthalmology will require a ~10x reduction in light exposure levels. A reduction of the imaging speed and an increase in the exposure time, combined with lower noise cameras and light sources, could improve the sensitivity to compensate lower permissible exposures. Moreover, extremely high density saturation mapping, as demonstrated here, may not be necessary in every clinical application. Rather, reliable measurements of regional saturation may also prove to be clinically relevant. Thus, spectra averaged over multiple axial scans at different locations in a single vessel, or at a single location in a vessel but averaged over time, could yield “point” measurements of oxygenation. On the other hand, light stimulation can induce changes in blood flow [53] and oxygen extraction fraction [54] in the inner retina. Hence, further development and validation of scanning protocols and algorithms in animal models is warranted before clinical translation.

### 5.6 Future work

Several potentially confounding effects were not accounted for in this work. Firstly, the saturation dependence of blood scattering [55] was not accounted for. However, as blood scattering is highly anisotropic (with a  $g$  factor of  $>0.95$  over the wavelength range of interest) a significant fraction of the forward scattered light is detected. Thus, the effective attenuation coefficient [56] of blood due to scattering is moderated by the high  $g$  value. Therefore, it remains unclear to what extent the saturation dependence of RBC scattering must be accounted for. Lastly, signal changes over the axial window (~22  $\mu\text{m}$ ) used for the STFT were not accounted for. For instance, variation in the mean backscattering due to RBC orientation or variations due to exponential attenuation can act as “window functions” that cause distortion of the measured spectrum, and hence lead to erroneous chromophore estimates. Orientation effects appeared to be particularly prominent in the retina (Fig. 7, Fig. 8, Fig. 11, and Fig. 12). In this study, we minimized these effects by performing measurements only at deep locations in vessels with high  $R^2$  values and large values of  $LC_{HbT}$ . A more prospective correction for this shaping effect will be the subject of a future study.

### Acknowledgments

We acknowledge support from the National Institutes of Health (R00NS067050), the American Heart Association (11IRG5440002), and the Glaucoma Research Foundation Catalyst for a Cure. We thank Bruce Rosen, Anna Devor, and Maria Angela Franceschini for general support and advice.